



Oxygen-vacancy-related dielectric relaxations and electrical properties in $[\text{Li}_x(\text{BaSrCaMg})_{(1-x)/4}]\text{TiO}_3$ high-entropy perovskite ceramics

Jun Zhang¹, Haowen Liu¹, Yaohang Gu¹, Jinrong Zhang¹, Xiaoyan Zhang^{1,3}, and Xiwei Qi^{2,*}

¹ School of Materials Science and Engineering, Northeastern University, Shenyang 110189, China

² College of Metallurgy and Energy, North China of Science and Technology, Tangshan 063210, China

³ School of Resources and Materials, Northeastern University at Qinhuangdao, Qinhuangdao 066004, China

Received: 13 January 2022

Accepted: 23 February 2022

Published online:
5 April 2022

© The Author(s), under exclusive licence to Springer Science+Business Media, LLC, part of Springer Nature 2022

ABSTRACT

High-entropy perovskite ceramics, $[\text{Li}_x(\text{BaSrCaMg})_{(1-x)/4}]\text{TiO}_3$ ($x = 0.1, 0.15, 0.2, 0.3$), were designed and successfully synthesized by solid-state method. The effects of Li contents on the phase formation, microstructures, and the origin of dielectric relaxation of all ceramics have been systematically investigated. The results show that all ceramics exhibit perovskite structure, and increasing Li content is conducive to grain growth and the formation of dense ceramics. XPS and EPR prove that oxygen vacancies increase with the increase of Li content. It is observed at room temperature that the increase of Li content not only contributes to the improved permittivity but also results in high-dielectric loss. Two sets of dielectric relaxations are observed in all ceramics. The lower temperature relaxation is shown to originate from the interfacial polarization, while the higher temperature relaxation is ascribed to double-ionized oxygen vacancies. The rapid increase of permittivity at higher temperatures and lower frequencies can be explained by space charge related to oxygen vacancies.

1 Introduction

In recent years, high entropy is a new material design paradigm, in which more and more researchers have designed high entropy materials reasonably and worked out the corresponding effective strategies. Inspired by the traditional concept of high-entropy alloys [1–3], high-entropy oxides with more complex and diverse crystal structures have become a research

hotspot [4–6]. In particular, high entropy oxides ceramics with rock salt structure have been first proposed by Rost et al. [7], and more and more high entropy oxide ceramics with other structures have been excavated. In the past several years, the research on high-entropy oxides has mainly concentrated on rock salt-type structures [8, 9], etc. Nevertheless, high-entropy perovskite ceramics can no longer be ignored due to their good structural stability and

Address correspondence to E-mail: qxw@mail.neuq.edu.cn

variety of excellent physical properties [4, 10]. Jiang et al. [4] successfully prepared high-entropy oxides with perovskite structure composed of 13 cations by combing mixed entropy, tolerance factor and atomic size difference. Sarkar et al. [11] successfully synthesized high-entropy perovskite ceramics in which the A-site and B-site were substituted by five different elements, and confirmed the existence of entropy-driven structural stability in this system. On this basis, Qi et al. [12] first applied high entropy perovskite oxides in the field of lithium-ion batteries, the excellent cycle stability and high rate performance are attributed to the entropy-stabilized structure and the charge compensation mechanism. Pu et al. [13] prepared $(\text{Na}_{0.2}\text{Bi}_{0.2}\text{Ba}_{0.2}\text{Sr}_{0.2}\text{Ca}_{0.2})\text{TiO}_3$ high entropy perovskite ceramics, which provide new ideas for the application of energy storage and electrothermal properties. A broader tolerance factor is a characteristic of perovskite structure and can be synergized by ions with different radii and valence states [4]. ABO_3 perovskite oxides have been widely applied in many fields, such as proton conductors [14], dielectric materials [15–21], ferroelectric materials [22–24]. Perovskite structural variants combined with high-entropy unique “four core effects” [5], accordingly, more excellent properties such as dielectric properties [25], superionic conductivity [26–28], and electrothermal properties [13] are urged to further exploration.

There are some breakthroughs in the research of high entropy perovskite ceramics, however, the research on its dielectric properties is still confined in a scarce stage. For the traditional perovskite SrTiO_3 ceramics, it is well known that the change of substitution-types will lead to the change of carrier relative concentration (such as oxygen vacancy), thus leading to the change of dielectric behavior [21]. From the perspective of defect design, in order to maintain the charge balance, oxygen vacancies (OVs) or defect dipole clusters are usually generated in the material, so as to improve the dielectric property [27, 29]. However, for the high entropy perovskite system, based on high configurational entropy ($\Delta S_{\text{conf}} > 1.5 \text{ R}$) and valence combinations [30–32], the relationships between acceptor elements and OVs were rarely reported.

Therefore, based on the above defect design analysis, a novel high-entropy oxide $[\text{Li}_x(\text{BaSrCaMg})_{(1-x)/4}]\text{TiO}_3$ with perovskite structure were designed and prepared by solid-state method. In this paper, the

dielectric relaxations to the high-entropy perovskite systems have been systematically investigated for the first time. Moreover, the effects of Li content on the phase structure, microstructure, and dielectric behavior of $[\text{Li}_x(\text{BaSrCaMg})_{(1-x)/4}]\text{TiO}_3$ ceramics were systematically studied.

2 Experiment

Analytically reagents Li_2O , BaO , SrCO_3 , CaO , MgO , and TiO_2 were selected as raw materials and weighted according to the stoichiometric ratios. $[\text{Li}_x(\text{BaSrCaMg})_{(1-x)/4}]\text{TiO}_3$ high entropy oxides ($x = 0.1, 0.15, 0.2, 0.3$, thereafter abbreviated as Li-10, Li-15, Li-20, Li-30, respectively) were prepared by traditional solid-state method. The raw materials, zirconia balls and anhydrous ethanol were mixed and milled for 16 h. After drying, the powders were calcined at 1250°C for 3 h, then grind again for 1 h. After adding 5% PVA and grinding for a certain time, the obtained powders sieving through 60-mesh screen were pressed into a mold with a diameter of 10 mm under the pressure of 3–5 MPa. The PVA was removed by holding at 500°C for 4 h. All samples were eventually heated at 1400°C for 3 h for sintering. In particular, in order to reduce the influence of Li_2O volatilization during sintering process, excess 2% mole of Li_2O is added in the proportioning process [12], and the volatilization of Li_2O is suppressed as much as possible by buried sintering.

X-ray diffraction (XRD, Smart Lab, RIGAKU, Japan) was used to analyze the phase structure, and the step size was 0.02° , The scanning speed is $8^\circ/\text{min}$, The scanning range was $20\text{--}80^\circ$. Scanning electron microscopy (SEM, EDS, SUPRA-55, ZEISS, Germany) was used to observe the microstructure of the ceramic samples. Before SEM test, in order to make the ceramic surface conduct electricity, it is necessary to spray gold for 180 s in vacuum. The grain size of SEM image is calculated by Nono Measure software. X-ray photoelectron spectroscopy (XPS, ESCALAB, 250Xi, Thermo, America) was used to detect the valence and content of elements. Electron paramagnetic resonance (A300-10/12, Bruker, Germany) was used to analyze the oxygen vacancies. Impedance analyzer (TH2839, Tonghui, China) equipped temperature measurement systems was used to test AC impedance, dielectric and AC conductivity in

frequency range (100 Hz ~ 1 MHz) and temperature range (30–650 °C).

3 Results and discussion

According to one of the definitions of high-entropy alloys, a solid solution with high configurational entropy ($> 1.5 R$) is often referred to as “high-entropy” [30]. When each component element forms a high-entropy solid solution, the mixing entropy is calculated by formula (1):

$$\Delta S_{\text{conf}} = -R \sum_{i=1}^N C_i \ln C_i \quad (1)$$

where R is the ideal gas constant ($8.314 \text{ Jmol}^{-1} \text{ K}^{-1}$), C_i is the mole fraction of the i th component. With the increase of x from 0.01 to 0.03, the mixing entropy of the four ceramic samples varied from 1.57 R to 1.61 R, indicating that all the ceramic samples met the conditions of high configurational entropy formation.

Figure 1 shows the X-ray diffraction patterns of the samples sintered at 1400 °C. It can be seen that there is no impurity peak in the whole XRD pattern, which indicates that four samples with different Li content form a single solid solution. Pure cubic structure SrTiO_3 (PDF#01-1018) is detected for all components. In addition, it is more reliable to use the tolerance factor (t) for perovskite oxides to determine whether a single-phase structure is formed [4, 30]. As early as 1926, Goldschmid proposed to use the concept of tolerance factor to predict the stability of perovskite structure [4]:

$$t = \frac{R_A + R_O}{\sqrt{2}(R_B + R_O)} \quad (2)$$

where R_A and R_B are the cationic radii at A-site and B-site respectively, R_O is the radii of oxygen ion [4]. According to previous reports, Jiang et al. pointed out that $t \approx 1$ is a necessary and insufficient condition for the formation of stable single-phase high entropy perovskite ceramics [4]. The tolerance factor of all samples calculated by formula (2) is between 0.91 and 0.94 and less than 1, which suggests that single-phase high-entropy perovskite ceramics can also be formed at lower tolerance factors. The mixing entropy and tolerance factors of all ceramics are listed in Table 1.

The relative density and shrinkage percentage of all ceramics sintered at 1400 °C with different Li content are shown in Fig. 2. The changes of relative density and shrinkage of materials keep consistent. The relative density of Li-10 ceramic is 84%, while the Li-30 ceramic increases to 96.2% with the increase of Li content. It is well known that Li_2O is an effective sintering aid, and we consider that the increase in density of $[\text{Li}_x(\text{BaSrCaMg})_{(1-x)/4}]\text{TiO}_3$ ceramics may be caused by Li_2O accelerating the elimination of pores and promoting the sintering of ceramics [33, 34]. The increase of ceramic density can also be observed in SEM (Fig. 3). The contact between Li-10 ceramic grains is not close, heterogeneous distribution of grain size and there existed voids obviously. It can be seen from particle size distribution in Fig. 4 that when $x = 0.01$, the minimum average grain size is about $3.82 \mu\text{m}$, and the abscissa has a larger numerical range, indicating that the uniformity of the grain size is poor. When x increases to 0.03, Li-30 ceramic is significantly larger, about $5.83 \mu\text{m}$. The results show that the grain size of ceramics increases significantly, which may be due to the increase of Li_2O that promotes the mobility of grain boundaries

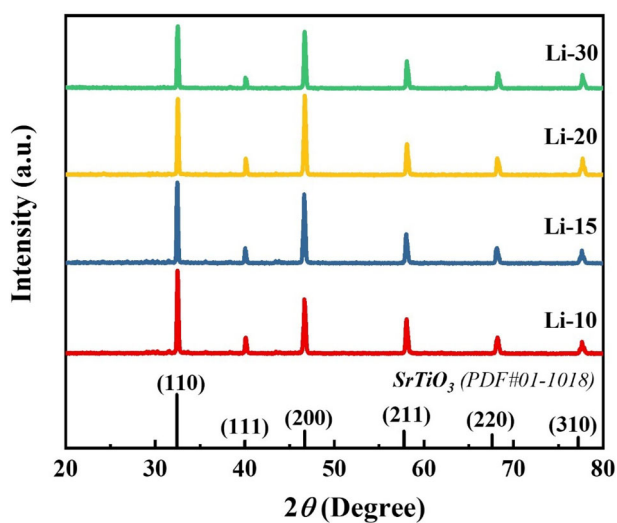


Fig. 1 XRD patterns of $[\text{Li}_x(\text{BaSrCaMg})_{(1-x)/4}]\text{TiO}_3$ ceramics

Table 1 Mixing entropy and tolerance factors of $[\text{Li}_x(\text{BaSrCaMg})_{(1-x)/4}]\text{TiO}_3$ ceramics with different components

x	Component	ΔS_{conf}	t
0.1	$[\text{Li}_{0.1}(\text{BaSrCaMg})_{0.225}]\text{TiO}_3$	1.57 R	0.9428
0.15	$[\text{Li}_{0.15}(\text{BaSrCaMg})_{0.2125}]\text{TiO}_3$	1.6 R	0.9358
0.2	$[\text{Li}_{0.2}\text{Ba}_{0.2}\text{Sr}_{0.2}\text{Ca}_{0.2}\text{Mg}_{0.2}]\text{TiO}_3$	1.61 R	0.9287
0.3	$[\text{Li}_{0.3}(\text{BaSrCaMg})_{0.175}]\text{TiO}_3$	1.58 R	0.9147

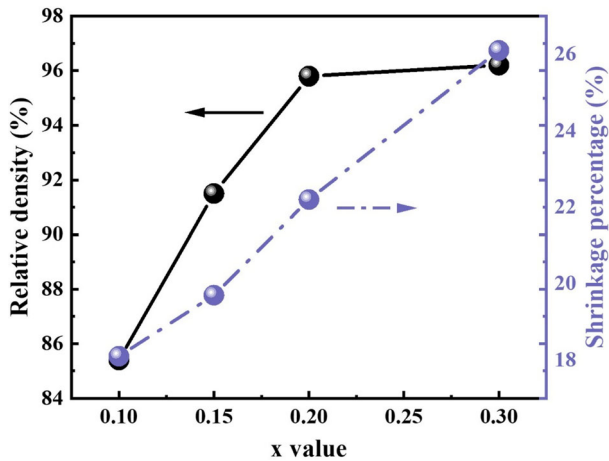


Fig. 2 Relationship between relative density and shrinkage percentage of $[\text{Li}_x(\text{BaSrCaMg})_{(1-x)/4}]\text{TiO}_3$ samples with different x values

and growth of grains [34, 35]. Meanwhile, the distribution of Li-30 ceramic is uniform, the contact between grains is close, and the voids are significantly reduced, which shows preferable compactness.

Frequency-dependent (10^2 – 10^6 Hz) permittivity and dielectric loss measured at room temperature are shown in Fig. 5. Both the permittivity and dielectric loss exhibit slightly frequency dispersion. At 100 Hz, the permittivity of Li-10 ceramic is 234 and the dielectric loss is 0.35, while the permittivity increases

to 584 for Li-30 ceramic and the dielectric loss reaches about 0.6. As the frequency of electric field increases, the permittivity decreases and presents a straight line at a higher frequency (10^5 – 10^6 Hz) as shown in the insert of Fig. 5, which shows good frequency stability in a wide frequency range. While the change of dielectric loss fails to keep up with the change of electric field, so the dielectric loss of various component is greatly decreased at a wide frequency, and maintained at the order of 10^{-3} – 10^{-4} .

Usually, low-frequency dielectric response is attributed to space charge polarization [36]. According to the perspective of defect design, the increase of dielectric loss may be due to the crucial role of acceptor Li^+ in $[\text{Li}_x(\text{BaSrCaMg})_{(1-x)/4}]\text{TiO}_3$ ceramics. The existence of low valence ions leads to oxygen vacancies in lattices to balance charges [27], which is induced when substituting a divalent cation “A” (Ba, Sr, Ca, Mg, respectively) by Li^+ [25, 37], as expressed in Eq. (3):



With the increase of Li content, more impurity defects appear in the crystal, resulting in more space charge in the ceramics, therefore, the higher dielectric loss in low frequency range may originate from space charge polarization [36, 38–40].

Due to the existence of acceptor Li, OV_s will inevitably be generated in $[\text{Li}_x(\text{BaSrCaMg})_{(1-x)/4}]\text{TiO}_3$

Fig. 3 SEM images of $[\text{Li}_x(\text{BaSrCaMg})_{(1-x)/4}]\text{TiO}_3$ samples. **a** Li-10; **b** Li-15; **c** Li-20; **d** Li-30

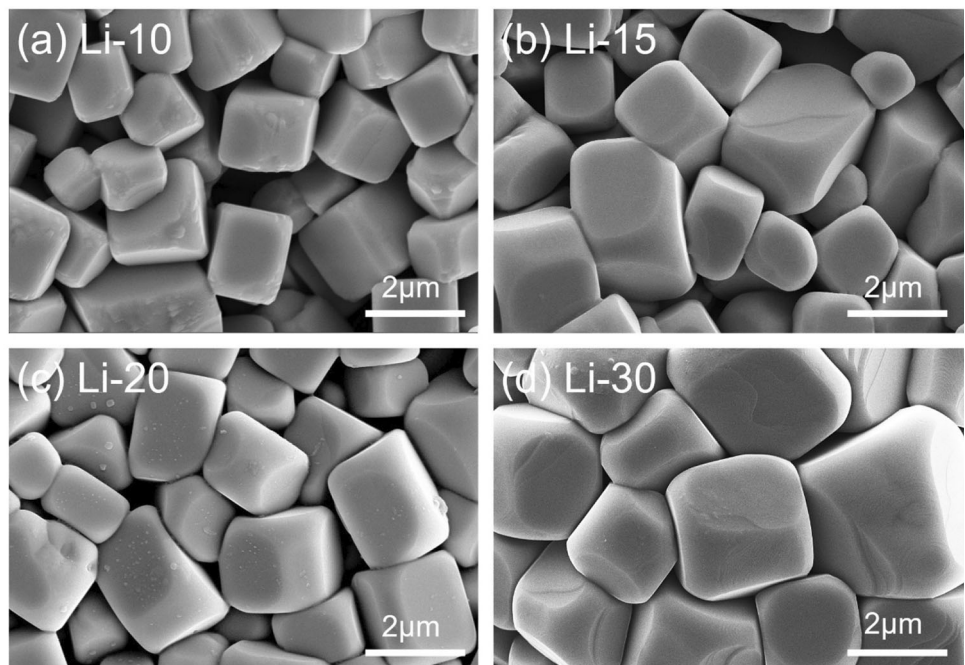


Fig. 4 Particle size distribution patterns of all samples. **a** Li-10; **b** Li-15; **c** Li-20; **d** Li-30

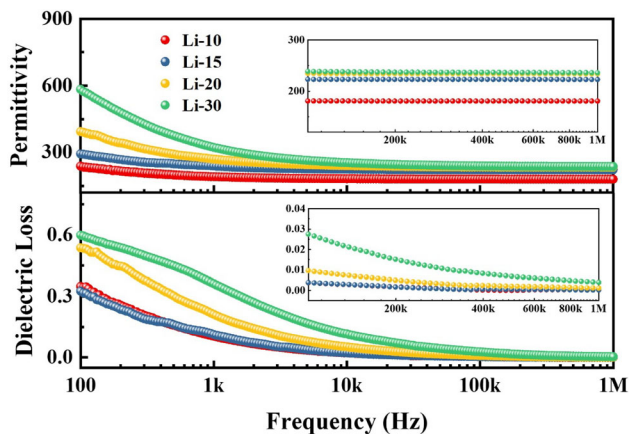
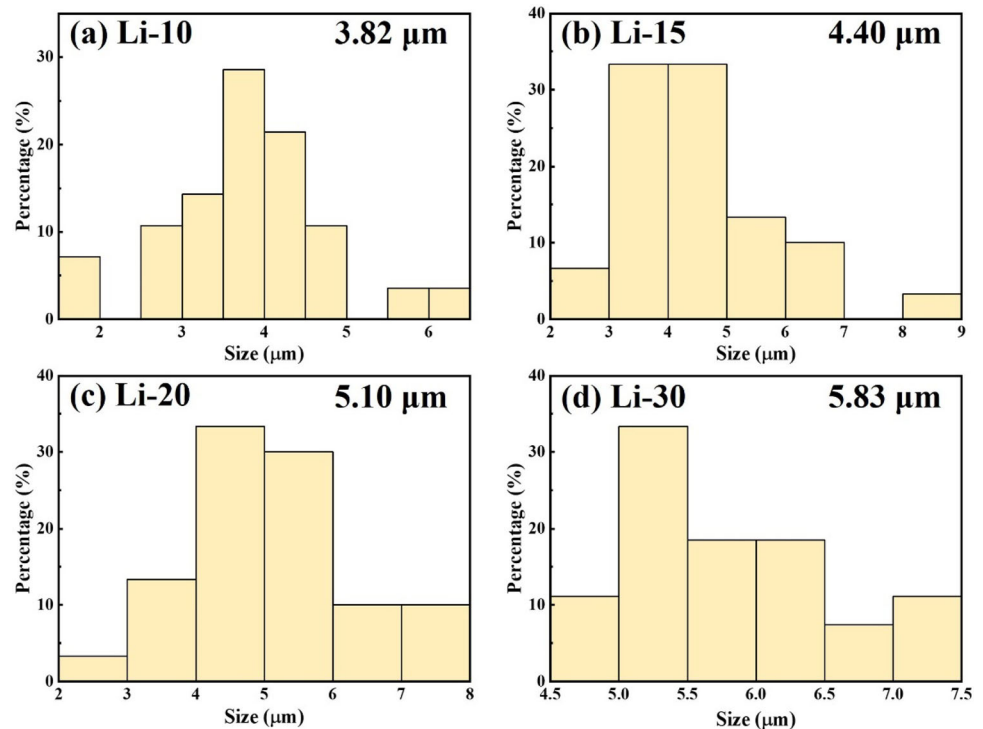


Fig. 5 Room temperature of the dielectric performance of $[\text{Li}_x(\text{BaSrCaMg})_{(1-x)/4}]\text{TiO}_3$, Insets are the local enlarged scale

$4]\text{TiO}_3$ ceramics to maintain charge neutrality, which are also known as extrinsic vacancies [41]. Since these OV are generated for charge compensation, the OV concentration cannot be changed by annealing in oxygen atmosphere [42]. Therefore, to investigate the changes of OV in $[\text{Li}_x(\text{BaSrCaMg})_{(1-x)/4}]\text{TiO}_3$ ceramics, the chemical valence state of oxygen element was verified by XPS. Figure 6 records the fitting results of O 1s peak of Li-30 ceramic, which is selected as a typical sample because of its best dielectric properties. The raw data can be ideally

fitted to three peaks, according to the literature reports, the peaks coordinated in the position around ~ 529.1 eV, ~ 530.2 eV and ~ 531.5 eV indicate lattice oxygen, vacancy oxygen and adsorbed H_2O related respectively [43, 44]. The existence of OV can be significantly observed from Fig. 6. Moreover, the insert in Fig. 6 shows the proportion between oxygen vacancies and lattice oxygen for all

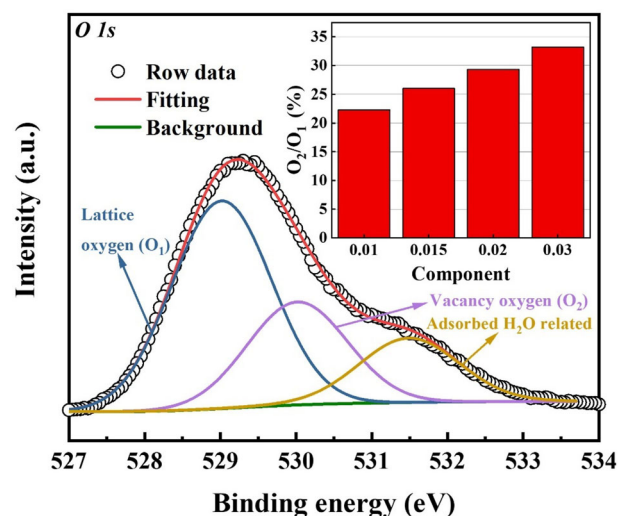


Fig. 6 XPS spectra of the O 1s peak of Li-30 ceramic. Insert is the proportion between oxygen vacancies and lattice oxygen for all ceramics

samples with different Li contents. The ratio of oxygen vacancies to lattice oxygen gradually increases with the increase of Li content, indicating that more acceptors increase the OV's of the lattice structure. EPR is a high efficiency means to detect some point defects in ceramics materials, which is adopted to supplied direct evidence of OV's defects in this work [21]. Room temperature EPR spectrum of all ceramics is recorded in Fig. 7. The signals at $g = 2.004$ can be ascribed to electrons capture on OV's, and the strength of peak at the signal is significantly stronger, which means that more OV's are generated [21].

The temperature dependence of the permittivity and dielectric loss of $[\text{Li}_x(\text{BaSrCaMg})_{(1-x)/4}]\text{TiO}_3$ ceramics at different frequencies are represented in Fig. 8. It can be obviously found that a favorable permittivity temperature stability of all samples at 30–150 °C, then increase rapidly with temperature increasing. This surge in permittivity is particularly pronounced at relatively low frequencies (< 10 kHz), whereas the permittivity is almost independent of temperature over a broad temperature range from 30 to 600 °C in 1 MHz. Moreover, the permittivity of each sample exhibits a decidedly dielectric anomaly with the temperature increasing, and with the increase of frequency, the critical temperature gradually shifts to higher temperature. The permittivity of Li-30 ceramic measured in 100 Hz has a peak at 522 °C (T_{peak}), as shown in the insert of Fig. 8g. The dielectric peaks of other three ceramics may appear at higher temperature due to the limited test temperature. Interestingly, all samples exhibit giant permittivity ($> 10^4$) at high temperature (> 400 °C) and low

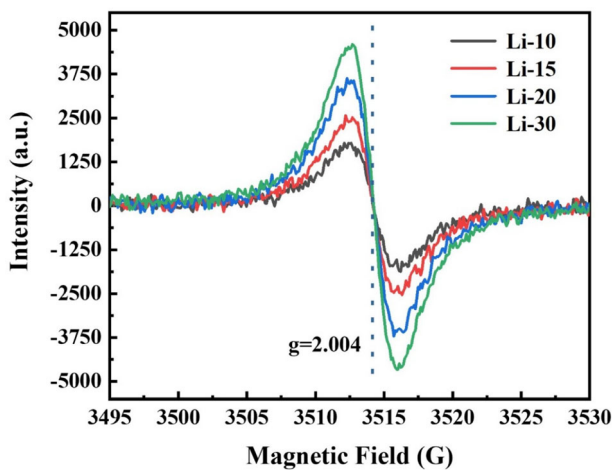


Fig. 7 Room temperature EPR spectrum of all ceramics

frequency (~ 100 Hz), the permittivity of Li-30 ceramic is close to 3×10^5 near 522 °C.

In addition, a dielectric loss peak near 150 °C can be observed from Fig. 8, and its position shifts to higher temperature with increasing frequency, which indicates an obvious thermally activated dielectric relaxation behavior [45]. However, the low frequency dielectric loss curves of all compositions show a rapid increasing background in high-temperature range, which is usually caused by the conductivity [41, 46, 47].

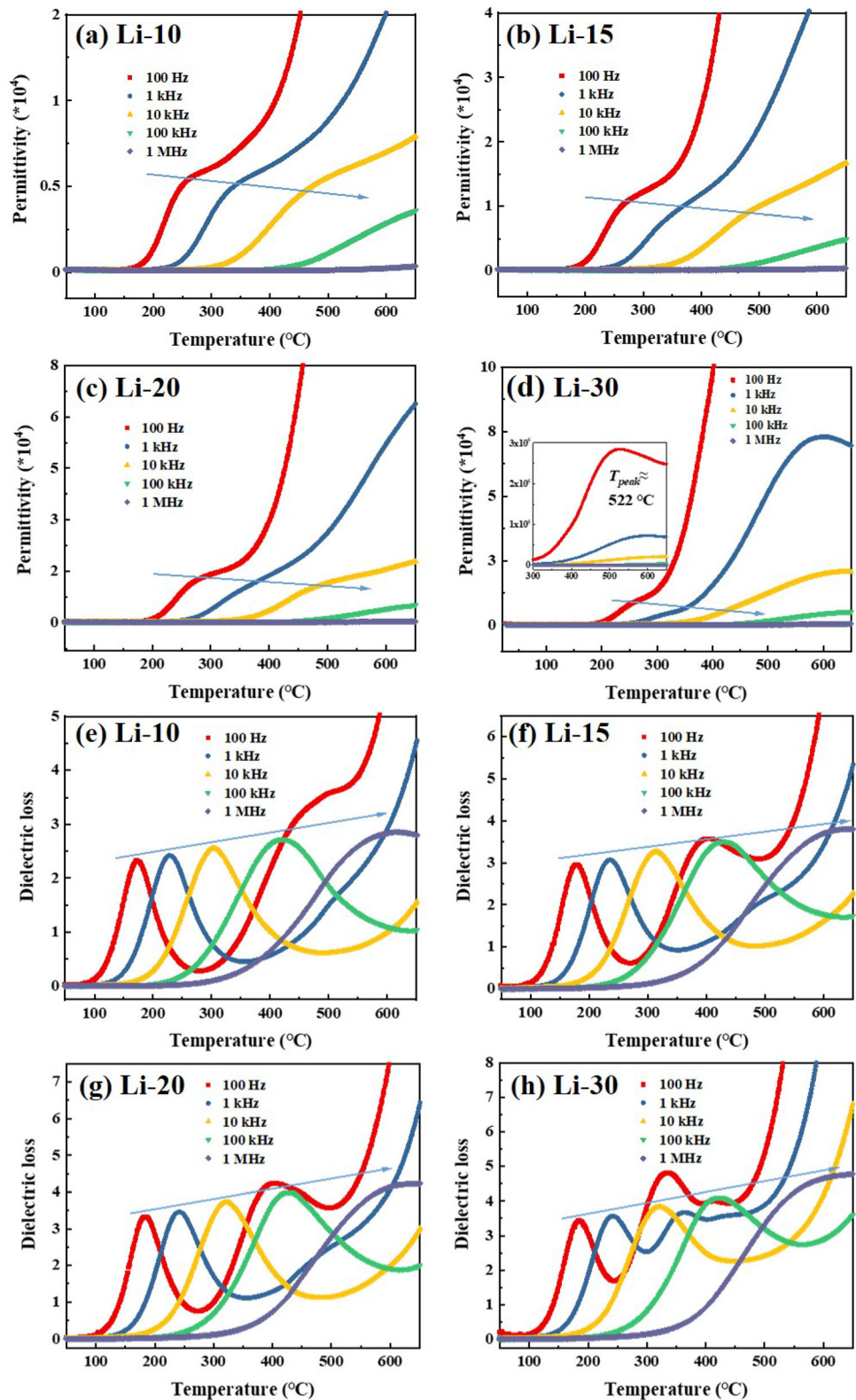
In particular, another dielectric relaxation peak occurs in the ceramics above 300 °C in 100 Hz, which indicates that two sets of dielectric relaxations are observed in ceramics. For simplicity, the low-and high-temperature relaxations are marked as LTR and HTR, respectively, as shown in Fig. 9a. It is noteworthy that the dielectric loss peaks of HTR gradually moves to a lower direction and the peak intensity increases significantly. According to the point defect theory, higher dielectric loss peaks demonstrate that higher concentration of relaxation units [48]. The common point of four ceramics is that OV's generated for insufficient charge compensation are the only variable, this implied that the LTR and HTR in all ceramics are mainly related to the OV's. In order to further reveal the relaxations processes, the Arrhenius formula is adopted to calculate the relaxation activation energies (E_a) for LTR. Figure 9b shows the functional relationship between $\ln f_p$ and $1000/T$, where T can be ideally obtained from the position of the loss peak in dielectric loss versus temperature curves, as shown in Eq. (4) [48]:

$$f_p = f_0 \exp(-E_a/kT) \quad (4)$$

where f_0 , E_a , and k are the pre-exponential factor, the relaxation activation energy and the Boltzmann constant, respectively. The observed activation energy for LTR, range of $E_a = 0.869$ eV ~ 0.931 eV, which approached that the typical value (1.0 eV) of E_a for OV's in perovskite structure ceramics [49]. Hence, we considered that the generation of LTR might be concerned with the migration of OV's in the ceramics [45].

To better comprehend the LTR mechanism and analyze the electrical properties of the ceramics, the complex impedance analysis provides an effective way to the relaxation process of grain and grain boundary are shown in Fig. 10a, in which the measurement frequency in the range of 100 Hz \sim 1 MHz

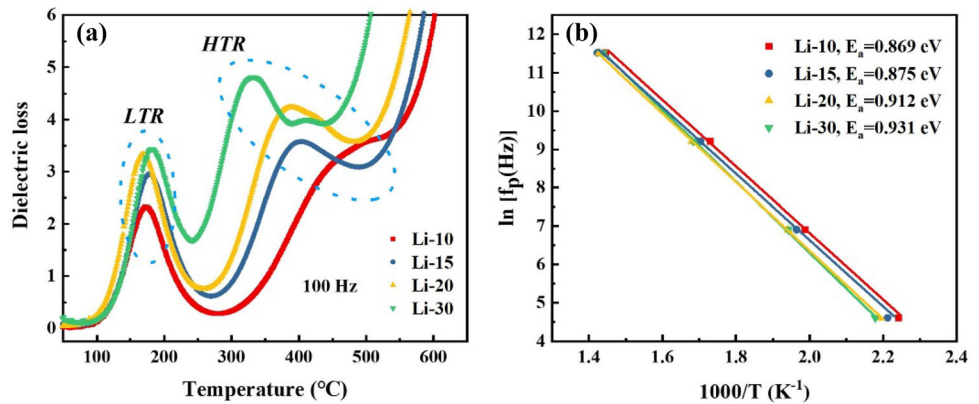
Fig. 8 Temperature dependent permittivity and dielectric loss of four ceramics. Insert in (g) is the local amplification



at 300 $^{\circ}\text{C}$. Two semicircles were observed in all ceramics, which generally indicates the generation of interfacial polarization. The larger-sized semicircle

corresponds to the response from grain boundary, while the smaller-sized one represents grain contribution [48]. The size of semicircle radius can roughly

Fig. 9 **a** Variation of dielectric loss of $[\text{Li}_x(\text{BaSrCaMg})_{(1-x)/4}]\text{TiO}_3$ ceramics with temperature at 100 Hz. **b** The Arrhenius plots of LTR of $[\text{Li}_x(\text{BaSrCaMg})_{(1-x)/4}]\text{TiO}_3$ ceramics



judge the insulation of samples, as shown in the inset of Fig. 10a. The semicircle corresponding to the grain boundary decreases significantly with the increase of Li content, indicating that the grain boundary insulation of the ceramics decreases gradually. Besides, the frequencies corresponding to the inflection points of the four arcs are 9120 Hz, 7586 Hz, 6607 Hz and 6310 Hz, respectively, which are consistent with the frequencies of dielectric loss peak shown in Fig. 10b. Therefore, it can be concluded that the LTR is due to the interfacial polarization between grain and grain boundary, which is caused by the motion of OVs there.

In order to further research the HTR, Fig. 11 shows the frequency dependence of ac conductivity for $[\text{Li}_x(\text{BaSrCaMg})_{(1-x)/4}]\text{TiO}_3$ ceramics measured at 400–650 °C. The conductivity increases with the increase of temperature, which can normally be explained by thermal activation of defect carriers (such as localized charge carries or OVs) [50]. Space charge mobility becomes easier as the temperature rises, and the charge carriers accumulated near the phase boundary have adequate energy to pass through the barrier constraints, resulting in an

enhanced conductivity [51]. When the samples have an inhomogeneous microstructure, due to the existence of two different conductive regions, the Maxwell–Wagner polarization or interfacial phenomena model usually exists in ceramics, which can be analyzed by ac conductivity [52]. It is worth nothing that the ac conductivity curve of Li-10 ceramic shows significant bending phenomenon at about 1 kHz and shifts to high frequency with the increase of temperature, indicating that the interfacial effect is evident. However, this bending phenomenon obviously decreases with the increase of Li content, and only a weak bend is observed in Li-30 ceramic at about 10 kHz, which indicates that the interfacial effect decreases gradually [52]. Therefore, it is reasonable to conclude that the Maxwell–Wagner polarization is not the main reason for the rapid increase of permittivity at higher temperature. Besides, in the low frequency region, the conductivity increases with the increase of temperature, decreases with the decrease of frequency, and approaches to a constant value, which can be regarded as the dc σ of grain boundary. Figure 12 shows the variations of dc σ with

Fig. 10 **a** Complex impedance spectra of samples measured at 300 °C. Insert is the amplified high frequency region. **b** Frequency dependence of dielectric loss for samples at 300 °C

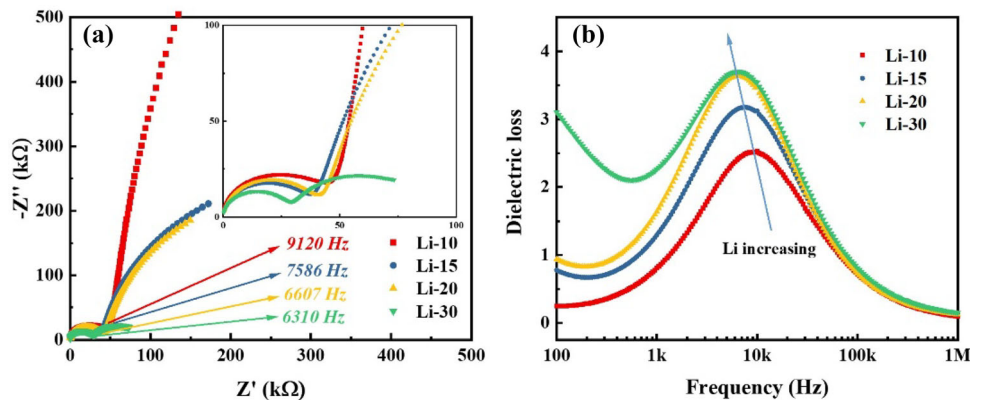
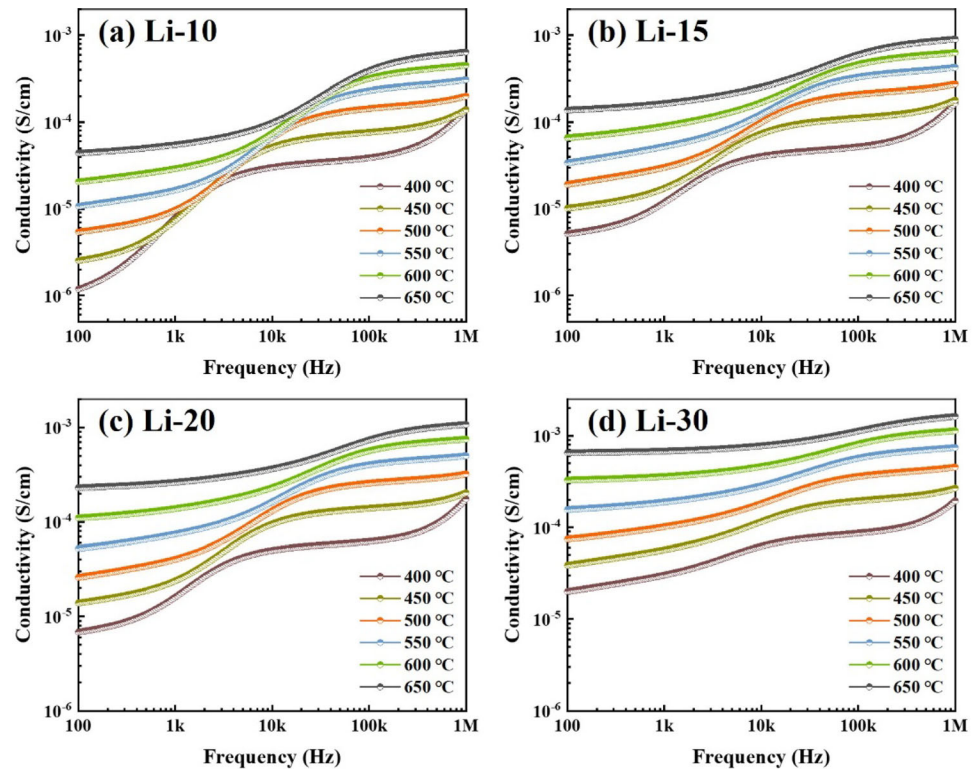


Fig. 11 The frequency dependence of ac conductivity for $[\text{Li}_x(\text{BaSrCaMg})_{1-x}]_4\text{TiO}_3$ ceramics measured at different temperature. **a** Li-10; **b** Li-15; **c** Li-20; **d** Li-30



corresponding $1/T$, which can be fitted with Arrhenius law [47]:

$$\sigma = \sigma_0 \exp(E_{\text{con}}/k_B T) \quad (5)$$

where σ_0 , E_{con} and k_B are the pre-exponential factor, the conductivity activation energy, and the Boltzmann constant, respectively. The dc σ conductivity can be estimated by ac conductivity data at the lowest frequency. According to Eq. (5), it can be calculated

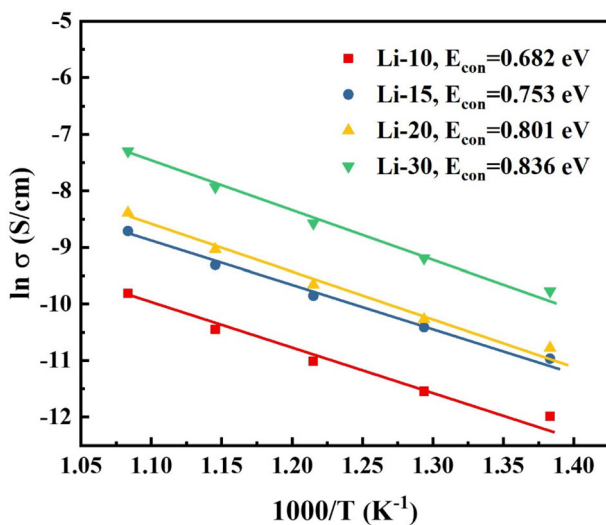
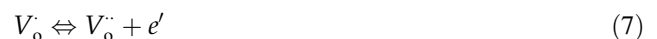


Fig. 12 Arrhenius plots of the dc conductivity for all samples

that the conductive activation energies of Li-10, Li-15, Li-20 and Li-30 samples in the same temperature range are 0.682 eV, 0.753 eV, 0.801 eV and 0.836 eV, respectively. In fact, the conduction of perovskite oxides at high temperature is generally ascribed to the conductive electrons generated by the ionization of OV [42], which can be written as:



where V_o^{2+} , V_o are double ionized and single ionized OVs, respectively. For perovskite oxides, whether it is relaxation activation energy or conductivity activation energy, it is composed of the activation energy of OVs. It is reported that the activation energies of single-ionized and double-ionized OVs range from 0.3 ~ 0.5 eV and 0.6 ~ 1.2 eV, respectively [53, 54]. Compare the E_{con} derived from the frequency-dependent of ac conductivity data with the E_a of double-ionized OVs, it can be concluded that the HTR is attributed to the double-ionized OVs [47].

It is well known that the dielectric relaxation of many perovskite oxides at high temperature can be explained by space charge model [55], which illustrates that increasing the concentration of OVs will cause the enhancement of conductivity and dielectric

relaxation [51]. Since the dielectric relaxation induced by OV is a diffusion-related process and the activated process is dependent on temperature [56]. OVs are “frozen-in” in low temperature, but they can be thermally “ionized” during high temperature [46, 56]. Obviously, OV-induced conduction occupies a dominant role in the high temperature and low frequency range, because the mobility and vacancy concentration, and the inertia of oxygen ions are higher at elevated temperatures [42, 46, 56]. Therefore, we consider that the rapid increase of permittivity at higher temperatures and lower frequencies should be attributed to space charge, which may be due to OVs and related defects.

4 Conclusion

High-entropy perovskite ceramics $[\text{Li}_x(-\text{BaSrCaMg})_{(1-x)/4}]\text{TiO}_3$ with the same perovskite structure were synthesized by traditional solid-state method and Li contents have significant influences on the microstructure, OV defects, and dielectric behaviors. Both the permittivity and dielectric loss exhibit slightly frequency dispersion at lower frequencies, while the permittivity display a weak frequency dependence from 100 kHz to 1 MHz. Two sets of relaxation peaks are observed in all samples, the LTR is attributed to the interfacial polarization, while the HTR arises from the double-ionized OVs. According to the impedance and ac conductivity analysis, it can be concluded that the Maxwell–Wagner polarization is not the main reason for the increase of permittivity. The rapid increase of permittivity at higher temperatures and lower frequencies can be explained by the space charge model, which is directly related to OVs introduced by the regulation of Li content.

Acknowledgements

This work was supported by National Natural Science Foundation of China under Grant (No. 51972048).

Author contributions

All authors contributed to the study conception and design. Material preparation, data collection and analysis were performed by JZ, the first draft of the manuscript was written by JZ and all authors commented on previous versions of the manuscript. All authors read and approved the final manuscript.

Funding

Funding was provided by National Natural Science Foundation of China (Grant Number 51972048).

Data availability

We confirm that material described in the manuscript, including all relevant raw data, will be freely available to any researcher wishing to use them for non-commercial purposes, without breaching participant confidentiality. The datasets generated during and/or analysed during the current study are available from the corresponding author on reasonable request.

Declarations

Conflict of interest We would like to declare on behalf of my co-authors that the work described is original research and has not been published previously, and not under consideration for publication elsewhere, in whole or in part. All the authors listed have approved the manuscript that is enclosed, and there is no conflict of interests during the submission of this manuscript. If accepted, this manuscript will not be published elsewhere in the same form, in English or in any other language, without the written consent.

References

1. Y.F. Ye, Q. Wang, J. Lu, C.T. Liu, Y. Yang, *Mater. Today* **19**, 349 (2016)
2. W. Huo, H. Zhou, F. Fang, Z. Xie, J. Jiang, *Mater. Des.* **134**, 226 (2017)
3. J.W. Yeh, S.K. Chen, S.J. Lin, J.Y. Gan, T.S. Chin, T.T. Shun, C.H. Tsau, S.Y. Chang, *Adv. Eng. Mater.* **6**, 299 (2004)
4. S. Jiang, T. Hu, J. Gild, N. Zhou, J. Nie, M. Qin, T. Harrington, K. Vecchio, J. Luo, *Scr. Mater.* **142**, 116 (2018)

5. H. Xiang, Y. Xing, F. zhi Dai, H. Wang, L. Su, L. Miao, G. Zhang, Y. Wang, X. Qi, L. Yao, H. Wang, B. Zhao, J. Li, Y. Zhou, *High-Entropy Ceramics: Present Status, Challenges, and a Look Forward* (2021).
6. M.R. Chellali, A. Sarkar, S.H. Nandam, S.S. Bhattacharya, B. Breitung, H. Hahn, L. Velasco, *Scr. Mater.* **166**, 58 (2019)
7. C.M. Rost, E. Sachet, T. Borman, A. Moballeggh, E.C. Dickey, D. Hou, J.L. Jones, S. Curtarolo, J.P. Maria, *Nat. Commun.* **6**, 1 (2015)
8. A. Sarkar, R. Djenadic, N.J. Usharani, K.P. Sanghvi, V.S.K. Chakravadhanula, A.S. Gandhi, H. Hahn, S.S. Bhattacharya, *J. Eur. Ceram. Soc.* **37**, 747 (2017)
9. M. Biesuz, L. Spiridigliozzi, G. Dell'Agli, M. Bortolotti, V.M. Sglavo, *J. Mater. Sci.* **53**, 8074 (2018)
10. H. Zhao, Y. Cheng, N. Xu, Y. Li, F. Li, W. Ding, X. Lu, *Solid State Ionics* **181**, 354 (2010)
11. A. Sarkar, R. Djenadic, D. Wang, C. Hein, R. Kautenburger, O. Clemens, H. Hahn, *J. Eur. Ceram. Soc.* **38**, 2318 (2018)
12. J. Yan, D. Wang, X. Zhang, J. Li, Q. Du, X. Liu, J. Zhang, X. Qi, *J. Mater. Sci.* **55**, 6942 (2020)
13. Y. Pu, Q. Zhang, R. Li, M. Chen, X. Du, S. Zhou, *Appl. Phys. Lett.* **115** (2019).
14. K.D. Kreuer, *Annu. Rev. Mater. Res.* **33**, 333 (2003)
15. W. Pan, M. Cao, C. Diao, C. Tao, H. Hao, Z. Yao, Z. Yu, H. Liu, *J. Mater. Sci.* **54**, 12401 (2019)
16. X. Zhang, J. Zhang, Y. Zhou, Z. Yue, L. Li, *J. Alloys Compd.* **767**, 424 (2018)
17. N. Wang, M. Cao, Z. He, C. Diao, Q. Zhang, Y. Zhang, J. Dai, F. Zeng, H. Hao, Z. Yao, H. Liu, *Ceram. Int.* **42**, 13593 (2016)
18. Z. Wang, M. Cao, Z. Yao, Q. Zhang, Z. Song, W. Hu, Q. Xu, H. Hao, H. Liu, Z. Yu, *J. Eur. Ceram. Soc.* **34**, 1755 (2014)
19. Z. Wang, M. Cao, Z. Yao, Z. Song, G. Li, W. Hu, H. Hao, H. Liu, *Ceram. Int.* **40**, 14127 (2014)
20. Z. Wang, Z. Wang, M. Cao, Z. Yao, H. Hao, Z. Song, X. Huang, W. Hu, H. Liu, *Ceram. Int.* **41**, 12945 (2015)
21. W. Pan, M. Cao, H. Hao, Z. Yao, Z. Yu, H. Liu, *J. Eur. Ceram. Soc.* **40**, 49 (2020)
22. K.F. Wang, J.M. Liu, Z.F. Ren, *Adv. Phys.* **58**, 321 (2009)
23. W. Kleemann, P. Borisov, S. Bedanta, V.V. Shvartsman, *IEEE Trans. Ultrason. Ferroelectr. Freq. Control* **57**, 2228 (2010)
24. A.A. Bokov, Z.G. Ye, *J. Mater. Sci.* **41**, 31 (2006)
25. D. Bérardan, S. Franger, D. Dragoe, A. K. Meena, N. Dragoe, *Phys. Status Solidi.* **10**, 328 (2016).
26. A. Sarkar, L. Velasco, D. Wang, Q. S. Wang, G. Talasila, L. de Biasi, C. Kubel, T. Brezesinski, S. S. Bhattacharya, H. Hahn, B. Breitung, *Nat. Commun.* **9** (2018).
27. N. Osenciat, D. Bérardan, D. Dragoe, B. Léridon, S. Holé, A.K. Meena, S. Franger, N. Dragoe, *J. Am. Ceram. Soc.* **102**, 6156 (2019)
28. D. Bérardan, S. Franger, A.K. Meena, N. Dragoe, *J. Mater. Chem. A* **4**, 9536 (2016)
29. Z. Rak, C. M. Rost, M. Lim, P. Sarker, C. Toher, S. Curtarolo, J. P. Maria, D. W. Brenner, *J. Appl. Phys.* **120** (2016).
30. S. Zhou, Y. Pu, Q. Zhang, R. Shi, X. Guo, W. Wang, J. Ji, T. Wei, T. Ouyang, *Ceram. Int.* **46**, 7430 (2020)
31. L. Tang, Z.M. Li, K.P. Chen, C.W. Li, X.W. Zhang, L.N. An, *J. Am. Ceram. Soc.* **104**, 1953 (2021)
32. J. Liu, G. Shao, D. Liu, K. Chen, K. Wang, B. Ma, K. Ren, Y. Wang, *Mater. Today Adv.* **8** (2020).
33. S. Le, S. Zhu, X. Zhu, K. Sun, *J. Power Sources* **222**, 367 (2013)
34. S.W. Seo, M.W. Park, J.S. Lee, *J. Nanosci. Nanotechnol.* **16**, 5320 (2016)
35. P.L. Chen, I.W. Chen, *J. Am. Ceram. Soc.* **79**, 1793 (1996)
36. W. Li, Z. Liu, F. Zhang, Q. Sun, Y. Liu, Y. Li, *Ceram. Int.* **45**, 11920 (2019)
37. E. Olsson, X. Aparicio-Anglès, N.H. De Leeuw, *Phys. Chem. Chem. Phys.* **19**, 13960 (2017)
38. W. Dong, W. Hu, A. Berlie, K. Lau, H. Chen, R.L. Withers, Y. Liu, *A.C.S. Appl. Mater. Interfaces* **7**, 25321 (2015)
39. W. Tuichai, S. Danwittayakul, N. Chanlek, P. Srepusharawoot, P. Thongbai, S. Maensiri, *RSC Adv.* **7**, 95 (2017)
40. D. A. Crandles, S. M. M. Yee, M. Savinov, D. Nuzhnyy, J. Petzelt, S. Kamba, J. Prokes, *J. Appl. Phys.* **119** (2016).
41. T.F. Zhang, X.G. Tang, Q.X. Liu, Y.P. Jiang, X.X. Huang, *J. Am. Ceram. Soc.* **98**, 551 (2015)
42. T.F. Zhang, X.G. Tang, Q.X. Liu, Y.P. Jiang, X.X. Huang, *J. Am. Ceram. Soc.* **98**, 551 (2014)
43. X. Guo, Y. Pu, W. Wang, J. Ji, M. Yang, R. Shi, J. Li, *J. Alloys Compd.* **818**, 152866 (2020).
44. C. Yang, M.Y. Tse, X. Wei, J. Hao, *J. Mater. Chem. C* **5**, 5170 (2017)
45. X. Wang, X. Lu, C. Zhang, X. Wu, W. Cai, S. Peng, H. Bo, Y. Kan, F. Huang, J. Zhu, *J. Appl. Phys.* **107**, 2 (2010)
46. C. C. Wang, C. M. Lei, G. J. Wang, X. H. Sun, T. Li, S. G. Huang, H. Wang, Y. D. Li, *J. Appl. Phys.* **113** (2013).
47. S. Huang, K.P. Su, H.O. Wang, S.L. Yuan, D.X. Huo, *Mater. Chem. Phys.* **197**, 11 (2017)
48. G. Li, H. Liu, H. Hao, J. Liu, Z. Chen, X. Huang, M. Cao, Z. Yao, *Ceram. Int.* **42**, 16782 (2016)
49. X. F. Wang, X. M. Lu, C. Zhang, X. B. Wu, W. Cai, S. Peng, H. F. Bo, Y. Kan, F. Z. Huang, J. S. Zhu, *J. Appl. Phys.* **107** (2010).
50. X. Sun, J. Deng, S. Liu, T. Yan, B. Peng, W. Jia, Z. Mei, H. Su, L. Fang, L. Liu, *Appl. Phys. A* **122**, 1 (2016)
51. T. F. Zhang, X. G. Tang, Q. X. Liu, Y. P. Jiang, X. X. Huang, Q. F. Zhou, *J. Phys. D* **49** (2016).

52. Z. Wang, M. Cao, Q. Zhang, H. Hao, Z. Yao, Z. Wang, Z. Song, Y. Zhang, W. Hu, H. Liu, J. Am. Ceram. Soc. **98**, 476 (2015)
53. X. Sun, J. Deng, L. Liu, S. Liu, D. Shi, L. Fang, B. Elouadi, Mater. Res. Bull. **73**, 437 (2016)
54. L.J. Liu, Y.M. Huang, Y.H. Li, M.X. Wu, L. Fang, C.Z. Hu, Y.Z. Wang, Physica B **407**, 136 (2012)
55. O. Bidault, P. Goux, M. Kchikech, M. Belkaoumi, M. Maglione, Phys. Rev. B **49**, 7868 (1994)
56. Y. Wu, M.J. Forbess, S. Seraji, S.J. Limmer, T.P. Chou, G.Z. Cao, J. Appl. Phys. **89**, 5647 (2001)

Publisher's Note Springer Nature remains neutral with regard to jurisdictional claims in published maps and institutional affiliations.